



**HAL**  
open science

## **Revealing topological phase in Pancharatnam-Berry metasurfaces using mesoscopic electrodynamics**

Zhanjie Gao, Sandeep Golla, Rajath Sawant, Vladimir Osipov, Gauthier Briere, Stephane Vezean, Benjamin Damilano, Patrice Genevet, Konstantin E Dorfman

► **To cite this version:**

Zhanjie Gao, Sandeep Golla, Rajath Sawant, Vladimir Osipov, Gauthier Briere, et al.. Revealing topological phase in Pancharatnam-Berry metasurfaces using mesoscopic electrodynamics. *Nanophotonics*, 2020, 9 (16), pp.4711-4718. <10.1515/nanoph-2020-0365>. <hal-03582593>

**HAL Id: hal-03582593**

**<https://hal.science/hal-03582593v1>**

Submitted on 21 Feb 2022

**HAL** is a multi-disciplinary open access archive for the deposit and dissemination of scientific research documents, whether they are published or not. The documents may come from teaching and research institutions in France or abroad, or from public or private research centers.

L'archive ouverte pluridisciplinaire **HAL**, est destinée au dépôt et à la diffusion de documents scientifiques de niveau recherche, publiés ou non, émanant des établissements d'enseignement et de recherche français ou étrangers, des laboratoires publics ou privés.



HAL Authorization

## Research Article

Zhanjie Gao, Sandeep Golla, Rajath Sawant, Vladimir Osipov, Gauthier Briere, Stephane Vezeian, Benjamin Damilano, Patrice Genevet\*, and Konstantin E. Dorfman\*

# Revealing topological phase in Pancharatnam-Berry metasurfaces using mesoscopic electrodynamics

<https://doi.org/>

Received Month DD, YYYY; revised Month DD, YYYY; accepted Month DD, YYYY

**Abstract:** Relying on the local orientation of nanostructures, Pancharatnam-Berry metasurfaces are currently enabling a new generation of polarization-sensitive optical devices. A systematical mesoscopic description of topological metasurfaces is developed, providing a deeper understanding of the physical mechanisms leading to the polarization-dependent breaking of translational symmetry in contrast with propagation phase effects. These theoretical results, along with interferometric experiment, contribute to the development of a solid theoretical framework for arbitrary polarization-dependent metasurfaces.

**Keywords:** mesoscopic electrodynamics, metasurface, Pancharatnam-Berry phase

## 1 Introduction

Pancharatnam-Berry (PB) metasurfaces, made of periodic arrangements of subwavelength scatterers or antennas, have been extensively studied over the last few years and are currently considered as a forthcoming substitute of bulky refractive optical components [1, 2]. The reflection and refractive properties of light at interfaces can be efficiently controlled by appropriately designing the phase

profile of these surfaces [3]. Several applications of PB metasurfaces, ranging from coloring to the realization of the multifunctional tunable/active wavefront shaping devices, have been proposed [4]. As a result of the fascinating degree of the wavefront manipulation offered by metasurfaces, this technology is currently bursting through the doors of industry, particularly driven by their potential application in redefining optical designs, such as lenses [5–8], holography [9–11], polarimetry [12–14] and a variety of broadband optical components, including free-form metaoptics [15–19].

Despite these applications, significant efforts are currently being made in deriving proper theoretical frameworks to guide the design of the complex components. Most of the disruptive attempts in controlling light-matter interactions rely on a fully vectorial [Maxwell's equations, such as effective medium theories \[20–22\]](#) and the comprehensive understanding of their polarization responses generally obtained using extensive numerical simulations, such as [finite element method \[23\]](#) or [finite-difference time domain techniques \[3, 24, 25\]](#), which often shows the exact simulation results but lacking of physical interpretations. Another approach, [Green's function method and diffraction theory for gratings, provides partial interpretation of a few diffractive properties of metasurfaces \[26–28\]](#). The generalized Snell's law can be then understood as a maximum grating efficiency in a given diffraction order [29, 30]. However, a vectorial theoretical framework is still required to clearly explain why the generalized Snell's law occurs in the cross-polarized transmitted fields in PB metasurface system in the -1st or 1st diffraction orders only. To overcome these difficulties, the concept of geometric phase (PB phase), which is responsible for the converted state of polarization in the linearly birefringent medium [32–36], is introduced. Several works have semi-theoretically shown that the transmission matrix which describes the birefringent response can be separated into co- and cross-polarized beams in the circular basis by applying the PB phase induced by the orientation of

---

\*Corresponding author: **Patrice Genevet**, Université Côte d'Azur, CNRS, CRHEA, rue Bernard Gregory, 06560 Valbonne, France, [patrice.genevet@crhea.cnrs.fr](mailto:patrice.genevet@crhea.cnrs.fr); and **Konstantin E. Dorfman**, State Key Laboratory of Precision Spectroscopy, East China Normal University, Shanghai 200062, China, [dorfman@ps.ecnu.edu.cn](mailto:dorfman@ps.ecnu.edu.cn)

**Zhanjie Gao, Vladimir Osipov**, State Key Laboratory of Precision Spectroscopy, East China Normal University, Shanghai 200062, China

**Sandeep Golla, Rajath Sawant, Gauthier Briere, Stephane Vezeian, Benjamin Damilano**, Université Côte d'Azur, CNRS, CRHEA, rue Bernard Gregory, 06560 Valbonne, France

**Zhanjie Gao**, and **Sandeep Golla** contributed equally to this work.

nano-antennas [31, 37, 38]. However, this approach does not originate from first principle derivation and is not capable of explaining other diffractive properties of PB metasurfaces, such as the connection between generalized Snell's law and polarization conversion. Obviously, each of these approaches just capture a part of the whole physical mechanism. To fill the gap between these concepts and incomplete demonstrations, a theoretical framework is highly needed to interpret all the diffractive properties of PB metasurfaces in a precise and systematic way.

In this letter, we propose a systematic mesoscopic electrodynamics theory to study the polarization-dependent metasurface, showing that the transmission of a co-polarized beam only acquires global phase associated with the antenna response, called "the propagation phase delay", while the transmission of a cross-polarized beam is sensitive to both PB and propagation phases. We extend this phase effect to a more general situation by decomposing the arbitrary polarization of a normally incident light in circular basis, showing that each eigenstate acquires an opposite phase delay due to the topological phase retardation associated with the PB phase (see Eq. 10). Furthermore, as a comprehensive theory, we derive a fully electro-dynamical expression and conduct optical measurements to analyze and validate this theoretical framework describing the diffractive properties of topological phase gradient metasurfaces [39, 40], including the physical mechanisms of the coexistence of the zero and nonzero phase gradient leading to the ordinary and generalized Snell's law, and the universal principles of co- and cross-polarization transmission.

## 2 The Mesoscopic Model

The topological phase occurring on the converted state of polarization is generated after transmission across a PB metasurface, as shown in Fig. 1A. To study these interface phenomenon, we consider non-magnetic PB metasurfaces and express the transmitted light starting from Maxwell's equations for monochromatic light in the media [41] (CGS units)

$$\Delta \mathbf{E} - \frac{\partial^2}{c^2 \partial t^2} \mathbf{E} = -4\pi \nabla (\nabla \cdot \mathbf{P}) + \frac{4\pi \partial^2}{c^2 \partial t^2} \mathbf{P}, \quad (1)$$

where we assume that the electric field  $\mathbf{E}$  with frequency  $\omega_i$  is far detuned from any electronic resonance and  $\mathbf{P}$  denotes the polarization of the metasurface and substrates on both side (see Section S1.A in Supplementary Materials (SM) for more details).

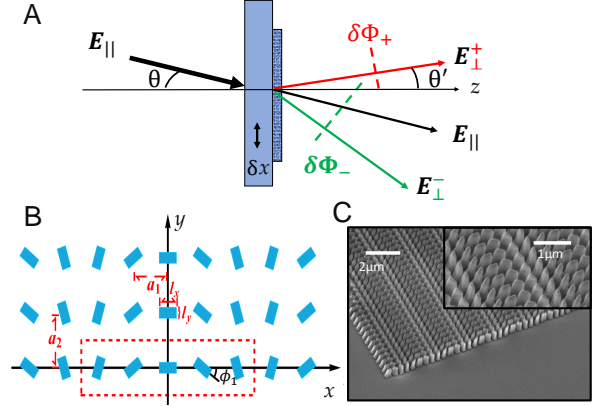


**Fig. 1:** (A) Schematic explaining the transmission properties of the PB metasurface where  $\mathbf{E}_{\parallel}$  and  $\mathbf{E}_{\perp}^{\pm}$  denote co- and cross-polarized beams,  $\theta$  and  $\theta'$  are the incident and refraction angles, respectively. (B) Schematic of the nanostructure array used to generate both classical and anomalous refraction. The array consists of a repetition of a unit cell containing five rotated nanopillars with dimensions  $l_x \times l_y \times l_z$  separated by subwavelength distances  $a_1$  and  $a_2$  along  $x$  and  $y$ , respectively. The first rotation angle is  $\phi_1 = \frac{-\pi}{2N+1}$ . (C) Scanning electron micrograph of a representative GaN-based PB metasurface.

The metasurface can be represented by a lattice with a primitive cell consisting of  $2N + 1$  Gallium Nitride (GaN) nanopillars distributed along the  $x$  coordinate, which corresponds to a reciprocal lattice vector  $\mathbf{G}_{mn} = \frac{2\pi m}{(2N+1)a_1} \mathbf{e}_x + \frac{2\pi n}{a_2} \mathbf{e}_y$ , where  $m, n$  are integers,  $a_1$  and  $a_2$  are the nearest spacing between the individual antennas along  $x$  and  $y$  directions, see Fig. 1B. The linear response of the individual antennas, at position  $j$  in the unit cell, is described by a polarization vector (see Section S1.B in SM for more details)

$$\mathbf{P}_j(z, \boldsymbol{\rho}, \omega) = N_0 \sum_{m,n} \int_{\mathbf{Q}} d^2 \boldsymbol{\kappa} f_{mn,j}(\phi_j) \mathbf{E}(z, \boldsymbol{\kappa}, \omega) e^{i\psi_{mn,j}}. \quad (2)$$

Here  $\psi_{mn,j} = \mathbf{G}_{mn} \cdot (\boldsymbol{\rho} - j\mathbf{a}_1) + \boldsymbol{\kappa} \cdot \boldsymbol{\rho}$  describes only the propagation phase, and the form-factor of the  $j$ -th element in the  $mn$ -th lattice unite cell is  $f_{mn,j}(\phi_j) = \tilde{\Omega}(\mathbf{G}_{mn}) / \pi(2N + 1)a_1a_2$  where  $\tilde{\Omega}(\mathbf{G}_{mn})$  is the Fourier transform of geometric shape factor  $\Omega(\boldsymbol{\rho}) = \mathcal{H}(|x| \leq l_x/2) \mathcal{H}(|y| \leq l_y/2)$  with Heaviside function  $\mathcal{H}(\text{condition}) = \{1, \text{ when condition is true}; 0, \text{ when condition is false}\}$ . The momentum integration over  $\boldsymbol{\kappa}$  runs over  $\mathbf{Q}$  - the first Brillouin zone. The coefficient  $N_0 = \frac{\chi_0}{8\pi^2}$  includes the antenna material susceptibility  $\chi_0$ .

The translational symmetry of the metasurface dictates the form of the solution which is given by

$$\mathbf{E}(z, \boldsymbol{\rho}) = \sum_{m,n} e^{i\mathbf{G}_{mn} \cdot \boldsymbol{\rho}} \int_{\mathbf{Q}} \frac{d^2\boldsymbol{\kappa}}{(2\pi)^2} \mathbf{E}_{mn}(z, \boldsymbol{\kappa}) e^{i\boldsymbol{\kappa} \cdot \boldsymbol{\rho}}. \quad (3)$$

Considering the thickness  $l_z$  to be much smaller than the  $xy$  dimension of the metasurface, we neglect the  $E_z$  and  $P_z$  components in the model. An incoming plane wave can be written as  $\mathbf{E}_{in}(z, \boldsymbol{\rho}) = \mathbf{E}_i e^{ik_z z + i\boldsymbol{\kappa}_i \cdot \boldsymbol{\rho}}$  where  $k_{zi} = \sqrt{\frac{\omega_i^2 n_i^2}{c^2} - \kappa_i^2}$  with propagation condition  $\omega_i n_i > c\kappa_i$  and refractive index  $n_i$ .

The geometric anisotropy of the antennas can be taken into account by replacing the scalar susceptibility  $\chi_0$  by the diagonal 2x2 susceptibility tensor. The tensor components along the  $x$  and  $y$  axes are given by  $\chi_x$  and  $\chi_y$ , respectively. Therefore, for the rectangular antenna oriented along  $x$  and  $y$ , the transmission matrix is given by  $\hat{\mathbf{E}} = \hat{\mathbf{T}} \mathbf{E}_i$ , where the transmitted electric field in the momentum space is  $\hat{\mathbf{E}} = \{\hat{E}_x, \hat{E}_y\}$ , and the incident field is  $\mathbf{E}_i = \{\tilde{E}_{xi}, \tilde{E}_{yi}\}$ . The transmission matrix then reads (see Section S2 in SM for details)

$$\hat{\mathbf{T}} = \begin{pmatrix} \tilde{t}_{xx} & \tilde{t}_{xy} \\ \tilde{t}_{yx} & \tilde{t}_{yy} \end{pmatrix}, \quad (4)$$

where  $\tilde{t}_{ij}$ ,  $i, j = x, y$  defined in Eq. (S17) explicitly depends on the form-factor  $f_{mn,j}$ . For the element oriented along  $x$  and  $y$  axes, i.e.  $\phi_j = 0$ , the corresponding form-factor  $f_{mn,j}(\phi_j = 0) \equiv \sin(\frac{ml_x \pi}{(2N+1)a_x}) \sin(\frac{nl_y \pi}{a_y}) / mn\pi^3$ . Since the metasurface consists of nanopillars rotated around  $z$  axes with the constant incremental angle  $\phi_j = \frac{-\pi j}{2N+1}$  in Fig. 1, the corresponding rotation matrix  $R(\phi_j)$  is given by

$$\hat{R}(\phi_j) = \begin{pmatrix} \cos(\phi_j) & -\sin(\phi_j) \\ \sin(\phi_j) & \cos(\phi_j) \end{pmatrix}, \quad (5)$$

According to superposition principle, the transmission matrix of the metasurface can be obtained by summing the contributions of individual antennas, given by  $\hat{\mathbf{E}}(\mathbf{K}) = \sum_j \hat{\mathbf{T}}'(\phi_j) \hat{\mathbf{E}}_i$ , where the rotation-dependent transmission matrix is given by  $\hat{\mathbf{T}}'(\phi_j) = \hat{R}^\dagger(\phi_j) \hat{\mathbf{T}} \hat{R}(\phi_j)$ .

Using Pauli algebra for two-component polarization basis without explicit factorization of the additional propagation phase, the rotation-dependent transmission matrix

reads

$$\begin{aligned} 2\hat{\mathbf{T}}'(\phi_j) &= (\tilde{t}_{xx} + \tilde{t}_{yy}) \hat{I} + i(\tilde{t}_{xy} - \tilde{t}_{yx}) \hat{\sigma}_z \\ &+ (\tilde{t}_{xx} - \tilde{t}_{yy})(e^{2i\phi_j} \hat{\sigma}_- + e^{-2i\phi_j} \hat{\sigma}_+) \\ &+ i(\tilde{t}_{xy} + \tilde{t}_{yx})(e^{2i\phi_j} \hat{\sigma}_- - e^{-2i\phi_j} \hat{\sigma}_+), \end{aligned} \quad (6)$$

Here,  $\hat{\sigma}_\pm = (\hat{\sigma}_x \pm i\hat{\sigma}_y)/2$  is the spin-flip operator and the extra phase term  $e^{\pm 2i\phi_j}$  can be understood as the PB phase term [31, 37, 38].

The transmitted field in the physical space (the form of  $\hat{\mathbf{T}}$  is listed in Eq. (S18)) can be consecutively written as  $\mathbf{E}(z, \boldsymbol{\rho}) = \sum_{mnj} F_{mn,j}(z, \boldsymbol{\rho}) \hat{\mathbf{T}}'(\phi_j) \mathbf{E}_i(z, \boldsymbol{\rho})$ , where the propagation factor is

$$F_{mn,j} = e^{i\psi_{mn,j}} [e^{ik_z z} \mathcal{H}(z > 0) + e^{-ik_z z} \mathcal{H}(z < 0)]|_{\boldsymbol{\kappa}=\boldsymbol{\kappa}_i}, \quad (7)$$

where  $k_z = \sqrt{\omega_i^2 n_i^2 / c^2 - K_{\parallel}^2}$ ,  $K_{\parallel}^2 = (G_{x,mn} + \kappa_x)^2 + (G_{y,mn} + \kappa_y)^2$  with momentum vectors of incident light  $\boldsymbol{\kappa}_i = \kappa_{xi} \mathbf{e}_x + \kappa_{yi} \mathbf{e}_y$ .

## 2.1 Discussion of analytical results

Analogous to the Bragg scattering in solid crystals, constructive interference of the propagating wave on the sub-wavelength periodic structure changes the complex amplitude of the refracted and reflected waves due to cumulative scattering from different crystal planes (see Eq. (7)). The evanescent waves emerge when  $n \neq 0$ , whose momentum vectors satisfy  $\omega_i^2 n_i^2 / c^2 - K_x^2 - K_y^2 < 0$ . Overall, the transmitted field with  $n = 0$  contains both effects of propagation and topological phases. The first line in Eq. (6) corresponding to the co-polarization component transmitted field contains only the propagation phase  $e^{i\psi_{mn,j}}$  embedded in the propagation factor  $F_{mn,j}$ . The second and the third lines in Eq. (6) yield the cross-polarization components which depend on both propagation and PB phases via  $e^{i\psi_{mn,j} \pm 2i\phi_j}$ . Due to the translation invariance, the PB phase of the individual antennas is distributed uniformly between 0 and  $2\pi$  such that  $\sum_j e^{\pm i\Xi_j} \simeq 0$  except  $m = 0, \pm 1$ , where  $\Xi_j = -\mathbf{G}_{mn} \cdot j\mathbf{a}_1 \pm 2\phi_j$  is the total constant phase. For  $m = 0$ , only the PB phase-independent co-polarized component can be observed. By calculating the  $x$ -dependent part of propagation phase  $\psi_{mn,j}$ , we can find this component corresponds to the conventional diffraction which follows the ordinary Snell's law,  $n_t \sin(\theta') - n_i \sin(\theta) = 0$  where  $\theta$  and  $\theta'$  are the incident and transmitted angles, respectively. For  $m = \pm 1$ , the PB phase cancels the  $j$ -dependent part of the propagation phase and only cross-polarized components are

detectable since  $G_{x,\pm 10}a_1j \equiv \mp 2\phi_j$ . The remaining  $x$ -dependent propagation phase given by  $(\frac{\pm 2\pi}{(2N+1)a_1} + \kappa_{xi})x$  yields the generalized Snell's law which governs the anomalous refraction. For the light beam propagating in the  $xz$  plane, the refraction angle is defined by  $\sin(\theta') = \frac{c}{\omega_i n_t} \left( \frac{\pm 2\pi}{(2N+1)a_1} + \kappa_{xi} \right)$ . Thus for  $x = [0, (2N+1)a_1]$ , one can obtain

$$\sin(\theta')n_t - \sin(\theta)n_i = \frac{\pm\lambda}{(2N+1)a_1}. \quad (8)$$

We now calculate the Fresnel coefficient and analyze the chiral transmission properties in the circular polarization (CP) basis:  $\sigma_{\pm} = (\mathbf{e}_x \cos(\theta') \pm i\mathbf{e}_y)/\sqrt{2}$  where  $\theta'$  is the refraction angle. Following the derivation shown in Section S3 and assuming the amplitude of the incident light is  $\mathbf{E}^s = \cos\theta\mathbf{e}_x + s i\mathbf{e}_y$  ( $s = \pm 1$ ), the transmitted light can be written as  $\mathbf{E} = \sum_{mnj} (\mathbf{E}_1 + \mathbf{E}_2 e^{-si2\phi_j} + \mathbf{E}_3 e^{si2\phi_j}) F_{mn,j}$ , where amplitudes  $\mathbf{E}_1$ ,  $\mathbf{E}_2$ , and  $\mathbf{E}_3$  are given by

$$\begin{aligned} \mathbf{E}_1 &= t_{1+}\mathbf{E}^s + t_{1-}\mathbf{E}^{-s}, \\ \mathbf{E}_2 &= t_{2-+}\mathbf{E}^s + t_{2++}\mathbf{E}^{-s}, \\ \mathbf{E}_3 &= t_{2+-}\mathbf{E}^s + t_{2--}\mathbf{E}^{-s}, \end{aligned} \quad (9)$$

Here, the coefficients  $t_{1\pm}$  and  $t_{2\pm\pm}$  are given in Eq. (S25). The additional phase factor  $e^{\pm si2\phi_j}$ , the PB phase, originates not only from the geometric rotation of the antenna in the unit cell, but also from the polarization of light. In other words, the additional phase  $\pm 2s\phi_j$  relies on the symmetry relation between the polarization of light and geometric nanostructures of metasurface rather than the specific coordinate system, which is a characteristic of topological phase. In order to make it more clear and easy to compare with existing research results, we discuss and summarize the selective transmission of cross-polarized beam for all possible chiral combinations of the input polarization and metasurface in Tab. 1. For the metasurface with clockwise rotating nanopillars depicted in Fig. 1B, right CP (RCP) incident light splits into RCP light and left CP (LCP) light, while LCP incident light splits into LCP light and RCP light. Furthermore, as we demonstrated here, the PB phase term  $e^{-si2\phi_j}$  of the output amplitude contributes to the effect of non-zero cross-polarized beam. If the entire metasurface is rotated counter-clockwise by  $\pi$  along  $z$  axis which means  $\phi_j = \frac{\pi}{2N+1}$ , the constant phase term is written as  $e^{2im\phi_j}$ . Then the phase gradient of cross-polarized beam changes its sign. It is clear that the sign of the phase gradient is determined by the handedness of incident light and metasurface.

For an arbitrary input polarization, we can decompose the normally incident light in the CP basis as  $\mathbf{E}_{in} \equiv \mathbf{E}_{||} = \alpha\sigma_+ + \beta\sigma_-$  with  $\beta = \sqrt{1 - \alpha^2}$  and considering a special

**Tab. 1:** Cross-polarized transmission for different combinations of the input polarization and metasurface

Antenna rotation	Input	Output (order)	Phase gradient
Clockwise	$\sigma_+$	$\sigma_-$ (+1)	$\frac{\lambda}{(2N+1)a_1}$
	$\sigma_-$	$\sigma_+$ (-1)	$\frac{-\lambda}{(2N+1)a_1}$
	LP	$\sigma_-$ (+1) $\sigma_+$ (-1)	$\frac{\lambda}{(2N+1)a_1}$ $\frac{-\lambda}{(2N+1)a_1}$
Counter-clockwise	$\sigma_+$	$\sigma_-$ (-1)	$\frac{-\lambda}{(2N+1)a_1}$
	$\sigma_-$	$\sigma_+$ (+1)	$\frac{\lambda}{(2N+1)a_1}$
	LP	$\sigma_-$ (-1) $\sigma_+$ (+1)	$\frac{-\lambda}{(2N+1)a_1}$ $\frac{\lambda}{(2N+1)a_1}$

LP denotes linear polarization.

setting  $\theta' = 0$ . The transmitted light can be then recast as

$$\mathbf{E} = \sum_{j,m=\pm 1} (t_{||} F_{00,j} \mathbf{E}_{||} + t_{\perp} F_{m0,j} M(\phi_j) \mathbf{E}_{\perp}), \quad (10)$$

where  $t_{||} = \frac{t_{xx} + t_{yy}}{2}$ ,  $t_{\perp} = \frac{t_{xx} - t_{yy}}{2}$ ,  $\mathbf{E}_{||} \cdot \mathbf{E}_{\perp} = 0$ , and  $M(\phi_j) = \begin{pmatrix} e^{i2\phi_j} & 0 \\ 0 & -e^{-i2\phi_j} \end{pmatrix}$ . The corresponding transmission of the co- and cross-polarized beams for an arbitrary polarization incident light are illustrated schematically in Fig. 1A. Depending on the combination of the incident polarization and geometric rotation of the antenna, a cross-polarized retardation with a positive or negative phase occurs, leading to self-constructive or self-destructive interference effects. Figure 1A indicates the relative phase retardation,  $\delta\Phi_{\pm}$ , is a function of the interface lateral displacement  $\delta(x)$  between co- and cross-polarized beams.

### 3 Interferometric measurement of the topological phase

Considering both polarization and rotation, the PB phase resulting in the opposite phase delays on the orthogonal CP components, and the new phenomena, such as generalized Snell's law, arbitrary polarization holography [6, 31], optical edge detection [42] and the photonic spin Hall effect [43, 44], are properly interpreted in our theoretical frame. In the following, we focus on topological phase characterization using the polarization-dependent translational symmetry breaking measurement based on the Mach-Zehnder interferometer (MZI). The GaN-based PB metasurface is used as a 50/50 CP beam splitter in the performance of self-phase referencing. To better understand the design of the birefringent nanostructure, we

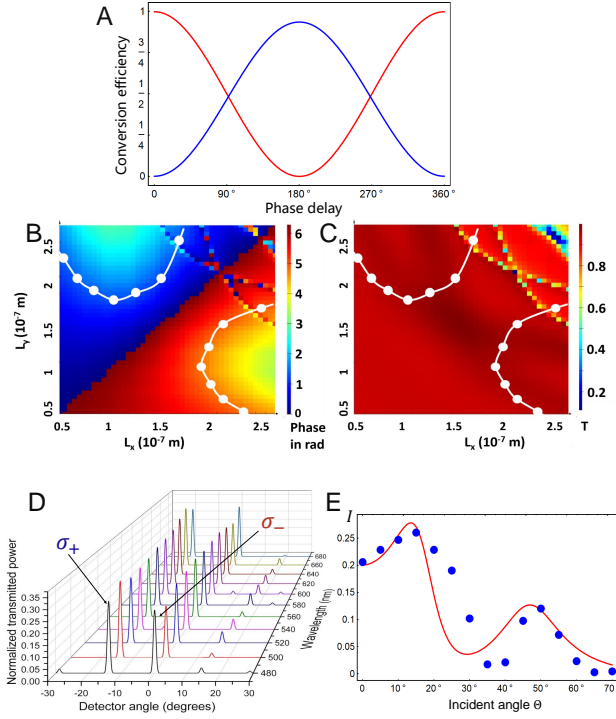


**Fig. 2:** (A) Calculated polarization conversion efficiency (blue), co-polarization transmission (red), of the subwavelength array of PB antennas as function of the delay between polarization eigenstates. (B) and (C) Full wave numerical simulations performed to extract the phase retardation between  $E_x$  and  $E_y$  components (B) and transmission maps (C) as functions of length and width of the nanopillars. (D) Experimental measurements of the normalized transmission across a PB metasurface designed according to the guideline in (B) and (C) as a function of the incidence angle changes for LCP ( $\sigma_-$ ) incidence. (E) Comparison between experiments and theory of the anomalous refraction efficiency as a function of the incident angle, where  $I$  is the transmitted power. Parameters of the simulations are  $a_1 = 500\text{nm}$ ,  $a_2 = 400\text{nm}$ ,  $l_x = 260\text{nm}$ ,  $l_y = 85\text{nm}$ ,  $l_z = 632.8\text{nm}$ ,  $\lambda = 632.8\text{nm}$ ,  $n_i = 1.61 + 0.3i$ ,  $n_t = 1.2 - 0.001i$ , and  $\chi_{x,y}$  (see Eq. (S8) in SM) with  $\omega_0 = 2.75\text{PHz}$ ,  $\omega_1 = 1.71\text{PHz}$ , and  $n_{\text{eff}} = 1.2 - 0.01i$  account for the Fresnel coefficient at the first interface (see Section S3.1 in SM for details).

theoretically calculate the co- and cross-polarized scattering amplitudes of an array of identical antennas as a function of the phase delay between  $x$  and  $y$  polarization, i.e. tuning the phase difference of the diagonal elements of susceptibility tensor which represents the geometric anisotropy of the metasurface. As shown in Fig. 2A, the ratio of the co- and cross-polarized transmission amplitude reach 50/50 when the phase difference of the diagonal elements of susceptibility tensor is  $\pi/2$  or  $3\pi/2$ . In order to identify GaN nanopillars with  $\pi/2$  or  $3\pi/2$  phase delay between  $x$  and  $y$  polarizations, full wave numerical simulations is performed to extract the phase

retardation between  $E_x$  and  $E_y$  components and also the transmission efficiency as functions of length and width of the nanopillars in Fig 2(B,C). The white lines indicate the regions for which the phase delay between  $x$  and  $y$  polarizations is equal to  $\pi/2$  and  $3\pi/2$ , which is crucial for the interferometric characterization of the PB phase. According to these theoretical prediction, dimensions of GaN nanopillars used were length  $l_x = 260\text{nm}$ ,  $l_y = 85\text{nm}$  and height  $800\text{nm}$ . These dimensions generate phase shift difference of  $3\pi/4$  between  $x$  and  $y$  axis. We create the arrays of rotated nanoantennas, each rotated by an angle  $\pi/5$  from its neighboring element as indicated in Fig. 1. The whole metasurface is of the size  $250\mu\text{m} \times 250\mu\text{m}$  array. The nanofabrication of metasurface was realized by patterning a  $800\text{nm}$  thick GaN thin film grown on a double side polished c-plan sapphire substrate via a Molecular Beam Epitaxy (MBE) RIBER system. The GaN nanopillars were fabricated using a conventional electron beam lithography system (Raith ElphyPlus, Zeiss Supra 40) process with metallic Nickel (Ni) hard masks through a lift-off process. To this purpose, a double layer of around  $200\text{nm}$  PMMA resists (495A4 then 950A2) was spin-coated on the GaN thin film, prior to baking the resist at a temperature of  $125^\circ\text{C}$ . E-beam resist exposition was performed at  $20\text{keV}$ . Resist development was realized with  $3 : 1$  IPA: MIBK and a  $50\text{nm}$  thick Ni mask was deposited using E-beam evaporation. After the lift-off process in the acetone solution for 4 hours, GaN nanopillar patterns were created using reactive ion etching (RIE, Oxford system) with a plasma composed of  $\text{Cl}_2\text{CH}_4\text{Ar}$  gases. Finally, the Ni mask on the top of GaN nanopillars was removed by using chemical etching with  $1 : 2$  solution of  $\text{HCl} : \text{HNO}_3$ .

Three gratings were designed and fabricated with different periodic arrangements of rotated antennas with periods  $2$ ,  $2.9$  and  $4\mu\text{m}$ , respectively. The metasurface refraction properties were characterized experimentally using a detector coupled to a lock-in amplifier that rotates in a circular motion, acquiring the refracted signal as a function of the transmission angle. To confirm the transmission properties of fabricated  $50/50$  PB metasurface beam splitter according to the theory prediction, spectral refraction response was obtained by sweeping the wavelength of a supercontinuum source coupled to a tunable single line filter in the range of  $480 - 680\text{nm}$ , by intervals of  $20\text{nm}$ . A linear polarizer followed by a quarter waveplate was utilized to select the state of the incident polarization. For the LCP (RCP) incidence on the metasurface, the transmission at the angle ranging from  $-30$  to  $30$  degrees was scanned as shown in Fig. 2D (Fig. S3). For normal LCP incident light, the zeroth order occurs at

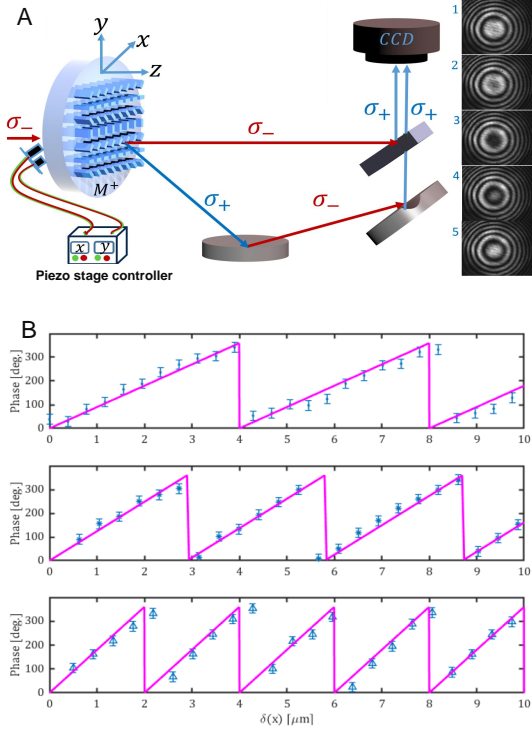


**Fig. 3:** (A) (Left) Schematic of the interferometric measurement for the characterization of the topological phase shift introduced by PB metasurface as a 50/50 CP beam splitter. Phase retardation of the anomalous refracted signal as a function of the lateral displacement of the metasurface, introduced by the shifting of metasurface along the phase gradient along the  $x$  axes, is recorded by monitoring the displacement of the interferogram fringes on a CCD camera after careful recombination and adjustment of the polarization handedness. (Right) The interference fringes displacement according to the phase gradient direction  $\delta x$ , resulting from the topological phase delay shift introduced on the anomalous beam. (B) The measured phase delays as a function of the displacements are reported for 3 different gratings, with periods  $\Gamma = 4, 2.9$  and  $2\mu\text{m}$  from top to bottom, respectively.

0 degrees. Both diffracted -1st (dominant) and 1st orders (weak residual signals at opposite refraction angle) are a consequence of the PB phase gradient. The amplitudes of these two dominant co-CP and cross-CP remain 50/50 when the incident wavelength changes as shown in Fig. 2D. To characterize the metasurface angular dispersion property, a detector is coupled to a lock-in amplifier that rotates in a circular motion. As shown in Fig. 2E, the experimentally measured transmission efficiency of cross-polarized beam has two well-resolved peaks around  $15^\circ$  and  $48^\circ$  which is in agreement with analytically predicted diffraction efficiency (red curve).

We have experimentally characterized the topological phase using a self-interferometric measurement in a MZI configuration, replacing a beam splitter by the metasurface

as shown in Fig. 3A. The measurements have been realized using a conventional diffraction setup, comprising a Si-detector plugged into a lock-in amplifier to improve the detection signal-to-noise ratio. The piezo stage controller is utilized to achieve minute translation of the metasurfaces as required for phase characterization in experiments discussed in Fig. 3B. In the present configuration, one arm of the MZI originates from the first order refraction from the metasurface. In addition to the anomalous refraction, the metasurface imposes a phase

$$\Phi_{\pm}(x) = G_{\pm 10,x}\delta(x), \quad (11)$$

which is proportional to the metasurface displacement  $\delta(x)$  along the phase gradient direction  $x$ . We propose to experimentally measure this phase by recombining both arms on a beam splitter, and recording the resulting intensity profile as a function of the translation distance. The transmitted light of RCP/LCP incidence is  $\mathbf{E} = \sum_j (t_{\parallel}\sigma_{\pm}e^{i\omega_i n_t z/c} - t_{\perp}e^{i\Phi_{\pm}(x)}\sigma_{\mp}e^{i\sqrt{\omega_i^2 n_t^2/c^2 - G_{\pm 10,x}^2}z})\mathcal{H}(z > 0)$ . The corresponding PB-dependent intensity measurement in the setup shown in Fig. 3A reads

$$I^+ = \frac{I_{\parallel} + I_{\perp}}{2}(1 + r \cos(\Phi_{\pm}(x))). \quad (12)$$

Here  $I_{\parallel} = |\sum_j t_{\parallel}|^2$ ,  $I_{\perp} = |\sum_j t_{\perp}|^2$  are the intensity of co- and cross-polarized transmission respectively, and  $r = \frac{\sqrt{I_{\parallel}I_{\perp}}}{I_{\parallel} + I_{\perp}}$ . Then the interference fringes displacement shown in right side of Fig. 3A provides indirect, yet unambiguous and conclusive measurement of the PB phase. As shown in Fig. 3B, we observe the linear phase variations with the wrapping periods equal to the PB phase of the metasurface in agreement with our theoretical result in Eq. (8).

## Conclusion

In summary, we provide an in-depth analysis of topological PB metasurfaces by comparing experimental results obtained with spatially oriented subwavelength birefringent nanostructures, with a mesoscopic theory. This work, which demonstrates the origin of both controllable phase retardation effects, namely the propagation phase and the PB phase, is a first step in developing an intuitive understanding of topological and functional beam splitters for future applications in quantum optics and their implementations in relevant quantum information protocols based on metasurfaces, which is an important future research direction in this field [45–51].

**Acknowledgment:** Z.G thanks S. Jiang, P. Saurabh, G. Zhu for valuable discussions. P.G, R.S, and G.B acknowledge funding from the European Research Council (ERC) under the European Union's Horizon 2020 research and innovation programme (Grant agreement no. 639109). Z.G, V.O and K.E.D gratefully acknowledge the support from National Science Foundation of China (No. 11934011), Zijiang Endowed Young Scholar Fund, East China normal University and Overseas Expertise Introduction Project for Discipline Innovation (111 Project, B12024).

## References

- [1] Genevet P, Capasso F, Aieta F, Khorasaninejad M, Devlin R. Recent advances in planar optics: from plasmonic to dielectric metasurfaces. *Optica* (2017);**4**:139-152.
- [2] Chen WT, Zhu AY, Sanjeev V, et al. A broadband achromatic metalens for focusing and imaging in the visible. *Nat Nanotechnol* (2018);**13**:220-226.
- [3] Yu N, Genevet P, Kats MA, et al. Light propagation with phase discontinuities: Generalized laws of reflection and refraction. *Science* (2011);**334**:333-337.
- [4] Kim I, Yoon G, Jang J, et al. Outfitting next generation displays with optical metasurfaces. *ACS Photonics* (2018);**5**:3876-3895.
- [5] Pors A, Nielsen MG, Eriksen RL, Bozhevolnyi SI. Broadband focusing flat mirrors based on plasmonic gradient metasurfaces. *Nano Letters* (2013);**13**:829-834.
- [6] Arbabi A, Horie Y, Bagheri M, Faraon A. Dielectric metasurfaces for complete control of phase and polarization with subwavelength spatial resolution and high transmission. *Nat Nanotechnol* **10** (2015), 937-943.
- [7] Khorasaninejad M, Chen WT, Devlin RC, et al., Metalenses at visible wavelengths: Diffraction-limited focusing and sub-wavelength resolution imaging. *Science* (2016);**352**:1190-1194.
- [8] Arbabi A, Arbabi E, Kamali SM, et al., Miniature optical planar camera based on a wide-angle metasurface doublet corrected for monochromatic aberrations. *Nat Commun* (2016);**7**:13682.
- [9] Chen WT, Yang K, Wang C, et al. High-efficiency broadband meta-hologram with polarization-controlled dual images. *Nano Letters* (2014);**14**:225-230.
- [10] Zheng G, Muhlenbernd H, Kenney M, et al. Metasurface holograms reaching 80% efficiency. *Nature Nanotechnol* (2015);**10**:308-312.
- [11] Ren H, Briere G, Fang X, et al. Metasurface orbital angular momentum holography. *Nat Commun* (2019);**10**:1-8.
- [12] Lin J, Mueller JPB, Wang Q, et al. Polarization-controlled tunable directional coupling of surface plasmon polaritons. *Science* (2013);**340**:331-334.
- [13] Ding F, Chen Y, Bozhevolnyi SI, Metasurface-based polarimeters. *Applied Sciences* (2018);**8**:594.
- [14] Rubin NA, Daversa G, Chevalier P, et al. Matrix fourier optics enables a compact full-stokes polarization camera. *Science* (2019);**365**.
- [15] Kamali SM, Arbabi A, Arbabi E, Horie Y, Faraon A, Decoupling optical function and geometrical form using conformal flexible dielectric metasurfaces. *Nat Commun* (2016);**7**:11618-11618.
- [16] Burch J, Wen D, Chen X, Falco AD. Conformable holographic metasurfaces. *Sci Rep* (2017);**7**:4520.
- [17] Burch J, Di Falco A. Surface topology specific metasurface holograms. *ACS Photonics* (2018);**5**:1762-1766.
- [18] Wu K, Coquet P, Wang QJ, Genevet P. Modelling of free-form conformal metasurfaces. *Nat Commun* (2018);**9**:1-8.
- [19] Dehmollaian M, Chamanara N, Caloz C. Wave scattering by a cylindrical metasurface cavity of arbitrary cross section: Theory and applications. *IEEE T Antenn Propag* (2019);**67**:4059-4072.
- [20] Roberts C, Inampudi S, Podolskiy V A. Diffractive interface theory: nonlocal susceptibility approach to the optics of metasurfaces. *Opt Express* (2015);**23**:2764-2776.
- [21] Achouri K, Caloz C. Design, concepts, and applications of electromagnetic metasurfaces. *Nanophotonics* (2018);**7**:1095-1116.
- [22] Momeni A, Rajabalipanah H, Abdolali A, Achouri K. Generalized optical signal processing based on multioperator metasurfaces synthesized by susceptibility tensors. *Phys Rev Appl* (2019);**11**:064042.
- [23] Khanikaev A, Arju N, Fan Z, et al. Experimental demonstration of the microscopic origin of circular dichroism in two-dimensional metamaterials. *Nat Commun* (2016);**7**:12045.
- [24] Sun S, He Q, Xiao S, Xu Q, Li X, Zhou L. Gradient-index meta-surfaces as a bridge linking propagating waves and surface waves. *Nat Mater*, (2012);**11**(5):426-431.
- [25] Vahabzadeh Y, Chamanara N, Caloz C, Generalized Sheet Transition Condition FDTD Simulation of Metasurface. *IEEE T Antenn Propag*, (2018);**66**(1):271-280.
- [26] De Abajo FJG. Colloquium : Light scattering by particle and hole arrays. *Rev Mod Phys* (2007);**79**:1267-1290.
- [27] Czaplicki R, Husu H, Siikanen R, et al. Enhancement of second-harmonic generation from metal nanoparticles by passive elements. *Phys Rev Lett* (2013);**110**:093902.
- [28] Liu W, Li Z, Cheng H, Chen S, Tian J. Momentum analysis for metasurfaces. *Phys Rev Appl* (2017);**8**:014012.
- [29] Smith DR, Tsai Y, Larouche S. Analysis of a gradient index metamaterial blazed diffraction grating. *IEEE Antenn Wirel Pr* (2011);**10**:1605-1608.
- [30] Larouche S, Smith DR. Reconciliation of generalized refraction with diffraction theory. *Opt Lett* (2012);**37**:2391-2393.
- [31] Mueller JPB, Rubin NA, Devlin RC, Groever B, Capasso F. Metasurface polarization optics: Independent phase control of arbitrary orthogonal states of polarization. *Phys Rev Lett* (2017); **118**:113901.
- [32] Pancharatnam S. Generalized theory of interference, and its applications: Part I. coherent pencils. *Proc Indian Acad Sci Sect A* (1956);**44**:247-262.
- [33] Berry MV. The adiabatic phase and pancharatnam's phase for polarized light. *J Mod Optic* (1987);**34**: 1401-1407.
- [34] Kuratsuji H, Kakigi S. Maxwell-schrodinger equation for polarized light and evolution of the stokes parameters. *Phys Rev Lett* (1998);**80**:1888-1891.
- [35] Bliokh KY, Bliokh YP. Conservation of angular momentum, transverse shift, and spin hall effect in reflection and

- refraction of an electromagnetic wave packet. *Phys Rev Lett* (2006);**96**:073903.
- [36] Zhu T, Lou Y, Zhou Y, et al. Generalized spatial differentiation from the spin hall effect of light and its application in image processing of edge detection. *Phys Rev Appl* (2019);**11**:034043.
- [37] Luo W, Xiao S, He Q, Sun S, Zhou L. Photonic spin hall effect with nearly 100% efficiency. *Adv Opt Mater* (2015);**3**:1102-1108.
- [38] Huang L, Chen X, Muhlenbernd H, et al. Dispersionless phase discontinuities for controlling light propagation. *Nano Lett* (2012);**12**:5750-5755.
- [39] Bomzon Z, Biener G, Kleiner V, Hasman E. Space-variant Pancharatnam-Berry phase optical elements with computer-generated subwavelength gratings. *Opt Lett* (2002);**27**:1141-1143.
- [40] Lin D, Fan P, Hasman E, Brongersma ML. Dielectric gradient metasurface optical elements. *Science* (2014);**345**:298-302.
- [41] Landau LD, Lifshitz EM. *Electrodynamics of continuous media*. (Pergamon, Amsterdam), Second edition, (1984).
- [42] Zhou J, Qian H, Chen C, et al. Optical edge detection based on high-efficiency dielectric metasurface. *Proc Natl Acad Sci USA* (2019);**116**:11137-11140.
- [43] Georgi P, Massaro M, Luo K, et al. Metasurface interferometry toward quantum sensors. *Light: Sci Appl* (2019);**8**:1-7.
- [44] Yin X, Ye Z, Rho J, Wang Y, Zhang X. Photonic spin hall effect at metasurfaces. *Science* (2013);**339**:1405-1407.
- [45] Liberal I, Engheta N. Nonradiating and radiating modes excited by quantum emitters in open epsilon-near-zero cavities. *Sci Adv* (2016);**2**.
- [46] Sokhoyan R, Atwater HA. Quantum optical properties of a dipole emitter coupled to an  $\epsilon$ -near-zero nanoscale waveguide. *Opt Express* (2013);**21**:32279-32290.
- [47] Ren X, Jha PK, Wang Y, Zhang X. Nonconventional metasurfaces: From non-hermitian coupling, quantum interactions, to skin cloak. *Nanophotonics* (2018);**7**:1233-1243.
- [48] Dorfman KE, Jha PK, Voronine DV, et al. Quantum-coherence-enhanced surface plasmon amplification by stimulated emission of radiation. *Phys Rev Lett* (2013);**111**:043601.
- [49] Jha PK, Ni X, Wu C, Wang Y, Zhang X. Metasurface-enabled remote quantum interference. *Phys Rev Lett* (2015);**115**:025501.
- [50] Lassalle E, Lalanne P, Aljunid S, Genevet P, Stout B, Durt T, Wilkowski D. Long-lifetime coherence in a quantum emitter induced by a metasurface. preprint (2019), <https://arxiv.org/pdf/1909.02409v1>.
- [51] Stav T, Faerman A, Maguid E, et al. Quantum entanglement of the spin and orbital angular momentum of photons using metamaterials. *Science* (2018);**361**:1101-1104.